

**Science**

 AAAS

**Self-Assembly of Ordered, Robust,  
Three-Dimensional Gold Nanocrystal/Silica Arrays**

Hongyou Fan, *et al.*  
*Science* **304**, 567 (2004);  
DOI: 10.1126/science.1095140

***The following resources related to this article are available online at  
www.sciencemag.org (this information is current as of December 21, 2007 ):***

**Updated information and services**, including high-resolution figures, can be found in the online version of this article at:

<http://www.sciencemag.org/cgi/content/full/304/5670/567>

**Supporting Online Material** can be found at:

<http://www.sciencemag.org/cgi/content/full/304/5670/567/DC1>

This article **cites 25 articles**, 7 of which can be accessed for free:

<http://www.sciencemag.org/cgi/content/full/304/5670/567#otherarticles>

This article has been **cited by** 99 article(s) on the ISI Web of Science.

This article has been **cited by** 1 articles hosted by HighWire Press; see:

<http://www.sciencemag.org/cgi/content/full/304/5670/567#otherarticles>

This article appears in the following **subject collections**:

Materials Science

[http://www.sciencemag.org/cgi/collection/mat\\_sci](http://www.sciencemag.org/cgi/collection/mat_sci)

Information about obtaining **reprints** of this article or about obtaining **permission to reproduce this article** in whole or in part can be found at:

<http://www.sciencemag.org/about/permissions.dtl>

RKKY interaction is not a settled matter (26).

Both single-dot and coupled-dot configurations (27) show roughly linear peak splitting as a function of in-plane magnetic field in the range  $B_{\parallel} \sim 2$  to 4 T, with slopes of  $\sim 70 \mu\text{eV/T}$ . This slope is larger by a factor of  $\sim 1.5$  than expected for the GaAs  $g$  factor of 0.44, but is consistent with  $g$ -factor measurements in other devices made from the same wafer. Both the single-dot and coupled-dot cases show an unexpected strengthening of the zero-bias peaks with  $B_{\parallel}$  before splitting is observed (for  $B_{\parallel} < 2$  T). This is not understood at present and will be investigated in more favorable device geometries in future work.

We have demonstrated coherent control of quantum dot spins by a nonlocal RKKY-like interaction. The present results suggest an approach to nonlocal control of spin and entanglement (28–30), which may be relevant to scaling of solid-state quantum information processing beyond the constraint of nearest-neighbor exchange.

#### References and Notes

1. An introductory review of the Kondo effect in quantum dots is available in L. Kouwenhoven, L. Glazman, *Physics World* **14**, 33 (2001).
2. L. I. Glazman, M. E. Raikh, *JETP Lett.* **47**, 452 (1988).
3. T. K. Ng, P. A. Lee, *Phys. Rev. Lett.* **61**, 1768 (1988).
4. Y. Meir, N. S. Wingreen, P. A. Lee, *Phys. Rev. Lett.* **70**, 2601 (1993).
5. D. Goldhaber-Gordon *et al.*, *Nature* **391**, 156 (1998).
6. A recent review of double quantum dots, with extensive citations to the literature, is available in W. G. van der Wiel *et al.*, *Rev. Mod. Phys.* **75**, 1 (2003).
7. H. Jeong, A. M. Chang, M. R. Melloch, *Science* **293**, 2221 (2001).
8. J. C. Chen, A. M. Chang, M. R. Melloch *Matter* **1**, cond-mat/0305289 (2003).
9. D. Loss, E. V. Sukhorukov, *Phys. Rev. Lett.* **84**, 1035 (2000).
10. D. Loss, D. P. DiVincenzo, *Phys. Rev. A* **57**, 120 (1998).
11. M. A. Ruderman, C. Kittel, *Phys. Rev.* **96**, 99 (1954).
12. T. Kasuya, *Prog. Theor. Phys.* **16**, 45 (1956).
13. K. Yosida, *Phys. Rev.* **106**, 893 (1957).
14. A. C. Hewson, *The Kondo Problem to Heavy Fermions* (Cambridge Univ. Press, Cambridge, 1993).
15. C. Jayaprakash, H. R. Krishnamurthy, J. W. Wilkins, *Phys. Rev. Lett.* **47**, 737 (1981).
16. B. A. Jones, C. M. Varma, *Phys. Rev. Lett.* **58**, 843 (1987).
17. B. A. Jones, C. M. Varma, *Phys. Rev. B* **40**, 324 (1989).
18. A. Georges, Y. Meir, *Phys. Rev. Lett.* **82**, 3508 (1999).
19. R. Aguado, D. C. Langreth, *Phys. Rev. Lett.* **85**, 1946 (2000).
20. W. Izumida, O. Sakai, *Phys. Rev. B* **62**, 10260 (2000).
21. T. Aono, M. Eto, *Phys. Rev. B* **63**, 125327 (2001).
22. R. Aguado, D. C. Langreth, *Phys. Rev. B* **67**, 245307 (2003).
23. V. N. Golovach, D. Loss, *Europhys. Lett.* **62**, 83 (2003).
24. Y. Utsumi, J. Martinek, P. Bruno, H. Imamura, *cond-mat/0310168* (2003).
25. The device was patterned using surface gates (Cr/Au) fabricated by electron-beam lithography. Peripheral dots have a lithographic area of  $0.25 \mu\text{m}^2$ ; the central dot has a lithographic area of  $0.35 \mu\text{m}^2$ . The device was fabricated on a delta-doped GaAs/AlGaAs heterostructure with electron gas 100 nm below the surface. Mobility  $2 \times 10^5 \text{ cm}^2/\text{Vs}$  and two-dimensional electron density  $2 \times 10^{11} \text{ cm}^{-2}$  give a transport mean free path of  $\sim 2.0 \mu\text{m}$  in the unpatterned material.
26. C. M. Varma, personal communication.
27. N. J. Craig *et al.*, data not shown.
28. T. J. Osborne, M. A. Nielsen, *Phys. Rev. A* **66**, 032110 (2002).

29. A. Saguia, M. S. Sarandy, *Phys. Rev. A* **67**, 012315 (2003).
30. F. Verstraete, M. Popp, J. I. Cirac, *Phys. Rev. Lett.* **92**, 027901 (2004).
31. We thank C. Varma, B. Halperin, and A. Yacoby for useful discussion. Supported in part by the Defense Advanced Research Projects Agency (DARPA)–Quantum Information Science and Technology (QUIST) program, the Army Research Office under DAAD-19-02-1-0070 and DAAD-19-99-1-0215, and

the NSF–Nanoscale Science and Engineering Center program at Harvard. Research at UCSB was supported in part by iQUIST. Supported by the Harvard College Research Program (N.J.C.), NSF (J.M.T.), and Middlebury College (E.A.L.).

8 January 2004; accepted 11 March 2004

Published online 25 March 2004;

10.1126/science.1095452

Include this information when citing this paper.

## Self-Assembly of Ordered, Robust, Three-Dimensional Gold Nanocrystal/Silica Arrays

Hongyou Fan,<sup>1,2\*</sup> Kai Yang,<sup>3</sup> Daniel M. Boye,<sup>4</sup> Thomas Sigmon,<sup>3</sup> Kevin J. Malloy,<sup>3</sup> Huifang Xu,<sup>2</sup> Gabriel P. López,<sup>2</sup> C. Jeffrey Brinker<sup>1,2\*</sup>

We report the synthesis of a new nanocrystal (NC) mesophase through self-assembly of water-soluble NC micelles with soluble silica. The mesophase comprises gold nanocrystals arranged within a silica matrix in a face-centered cubic lattice with cell dimensions that are adjustable through control of the nanocrystal diameter and/or the alkane chain lengths of the primary alkanethiol stabilizing ligands or the surrounding secondary surfactants. Under kinetically controlled silica polymerization conditions, evaporation drives self-assembly of NC micelles into ordered NC/silica thin-film mesophases during spin coating. The intermediate NC micelles are water soluble and of interest for biolabeling. Initial experiments on a metal-insulator-metal capacitor fabricated with an ordered three-dimensional gold nanocrystal/silica array as the “insulator” demonstrated collective Coulomb blockade behavior below 100 kelvin and established the current-voltage scaling relationship for a well-defined three-dimensional array of Coulomb islands.

Despite recent advances in the synthesis and characterization of nanocrystals and NC arrays (1, 2), there remain numerous challenges that limit their practical use. First, for example, synthesis procedures generally used for metallic and semiconducting NCs use organic passivating ligands that make the NCs water insoluble. This is problematic for biological imaging and more generally for uniform incorporation of nanocrystals in hydrophilic matrices like silica or titania needed for the fabrication of robust, functional lasers (3, 4). Second, while steric stabilization of nanocrystals with organic passivating layers suppresses attractive particle-particle interactions, thereby facilitating self-assembly of NC arrays, it necessarily causes the arrays to be mechanically weak and often thermally

and chemically unstable. Third, although evaporation of NC dispersions has been used to prepare quasi-3D NC arrays (5) and films containing isolated 3D NC islands (6), there exist no procedures to reliably fabricate 3D NC arrays as uniform thin films. These combined factors ultimately limit routine integration of nanocrystals into 3D artificial solid devices, in which electronic, magnetic, and optical properties could be tuned through electron charging and quantum confinement of individual NCs mediated by coupling interactions with neighboring NCs (7, 8).

Here, we describe the direct synthesis of water-soluble NC gold micelles and their further self-assembly with silica into robust, ordered 3D NC arrays in bulk or thin-film forms. The synthetic approach is general and avoids the complicated multistep procedures reported previously (9). Our concept is to consider monosized, organically passivated NCs as large hydrophobic molecules that, if incorporated individually into the hydrophobic interiors of surfactant micelles, would result in the formation of monosized NC micelles composed of a metallic (or other) NC core and a hybrid bilayer shell with precisely defined primary and secondary layer thicknesses (Fig. 1H). The hydrophilic NC

<sup>1</sup>Sandia National Laboratories, Chemical Synthesis and Nanomaterials Department, Advanced Materials Laboratory, 1001 University Boulevard SE, Albuquerque, NM 87106, USA. <sup>2</sup>The University of New Mexico/NSF Center for Micro-Engineered Materials, Department of Chemical and Nuclear Engineering, and <sup>3</sup>Center for High Technology Materials, Albuquerque, NM 87131, USA. <sup>4</sup>Physics Department, Davidson College, Davidson, NC 28035, USA.

\*To whom correspondence should be addressed. E-mail: hfan@sandia.gov (H.F.), cjbrink@sandia.gov (C.J.B.)

micelle surfaces provide water solubility and allow further assembly or derivatization as depicted in Fig. 1.

To individually incorporate NCs in surfactant micelles, we developed a microemulsion procedure (fig. S1) (10). A concentrated nanocrystal solution, prepared in organic solvent (e.g., chloroform, hexane), is added to an aqueous solution of surfactant with a volume ratio of 1:10 under vigorous stirring to create an oil-in-water microemulsion. Organic solvent evaporation (aided optionally by vacuum or heat treatments) transfers the NCs into the aqueous phase by an interfacial process driven by the hydrophobic van der Waals interactions between the primary alkane of the stabilizing ligand and the secondary alkane of the surfactant, resulting in thermodynamically defined interdigitated bilayer structures (Fig. 1H and fig. S1). For single-tailed

surfactants, an alkane chain of eight or more carbons is required to form micelles with gold nanocrystals stabilized by  $C_{12}$  alkanethiols [dodecanethiol (DT)]. Cationic, anionic, and nonionic surfactants, as well as phospholipids, can all form NC micelles (fig. S2), allowing facile control of micelle surface charge and functionality. In addition, fluorescent semiconducting CdSe NCs (stabilized by trioctylphosphine oxide) have been formed into NC micelles with maintenance of optical properties, further supporting the general nature and flexibility of this approach.

The formation and stability of individual gold NC micelles (as opposed to aggregated dimers, trimers, etc.) was confirmed by ultraviolet (UV)-visible spectroscopy and transmission electron microscopy (TEM), where we observed no difference between the positions and widths of the

plasmon resonance bands ( $\sim 510$  nm) of the  $C_{12}$ -alkanethiol-stabilized gold NCs in chloroform and those of the corresponding water-soluble NC micelles (Fig. 1D). In addition, evaporation of the NC micelle solutions resulted in self-assembly of hexagonally ordered NC arrays (Fig. 1C) as expected for individual, monosized nanocrystals. Judging from UV-visible spectroscopy and TEM and the ability to make ordered arrays, these solutions were stable for more than 2 years at room temperature.

In aqueous media, NC micelles organize hydrophilic components/precursors at the surfactant/water interface through electrostatic and hydrogen-bonding interactions by a mechanism analogous to that of surfactant-directed self-assembly of silica/surfactant mesophases (used as precursors to so-called "mesoporous silicas") (11). For example, addition of tetraethyl orthosilicate (TEOS) under basic conditions produced hydrophilic oligosilicic acid species that organize with NC micelles to form an ordered gold NC/silica mesophase with face-centered cubic (FCC) symmetry (space group  $Fm\bar{3}m$ ). Figure 2A, curve b, shows a representative low-angle x-ray diffraction (XRD) pattern of an NC mesophase powder prepared according to pathway i-ii-iii (Fig. 1) by using 2-nm-diameter  $C_{12}$ -thiol-stabilized gold NCs, cetyltrimethylammonium bromide ( $C_{16}$ TAB) surfactants, and sodium hydroxide catalyst. On the basis of FCC symmetry, the primary peaks are assigned as 111, 220, and 311 reflections. Figure 3, A and B, shows representative TEM images of [001]- and [012]-oriented NC mesophases (prepared as for Fig. 2A, curve b) along with their corresponding electron diffraction patterns. The TEM images are consistent with a unit cell with  $a = \sim 10.2$  nm and a uniform, minimum (silica/surfactant) spacing between NCs of  $\sim 6$  nm. This ordered nanocrystal array was formed spontaneously by self-assembly in aqueous media [rather than by solvent evaporation (12)]. Compared with other ordered NC arrays, the embedding silica matrix provides for greater chemical, mechanical, and thermal robustness and, compared with other connected NC systems [for example, those prepared by DNA hybridization (13, 14)], thermodynamically controlled self-assembly provides greater order and control of NC spacing.

Reducing the concentration of the gold NCs, while maintaining a constant surfactant/silica molar ratio, caused the progressive transformation of the cubic, gold NC/silica mesophase to a 2D hexagonal silica/surfactant mesophase (Fig. 2A, curves c and d), as is evident from the greatly diminished (111) reflection in XRD pattern (d) and the appearance of (100), (110), (200), and (210) reflections [Fig. 2A, curve d and magnified inset]. The highly ordered gold NC/silica array

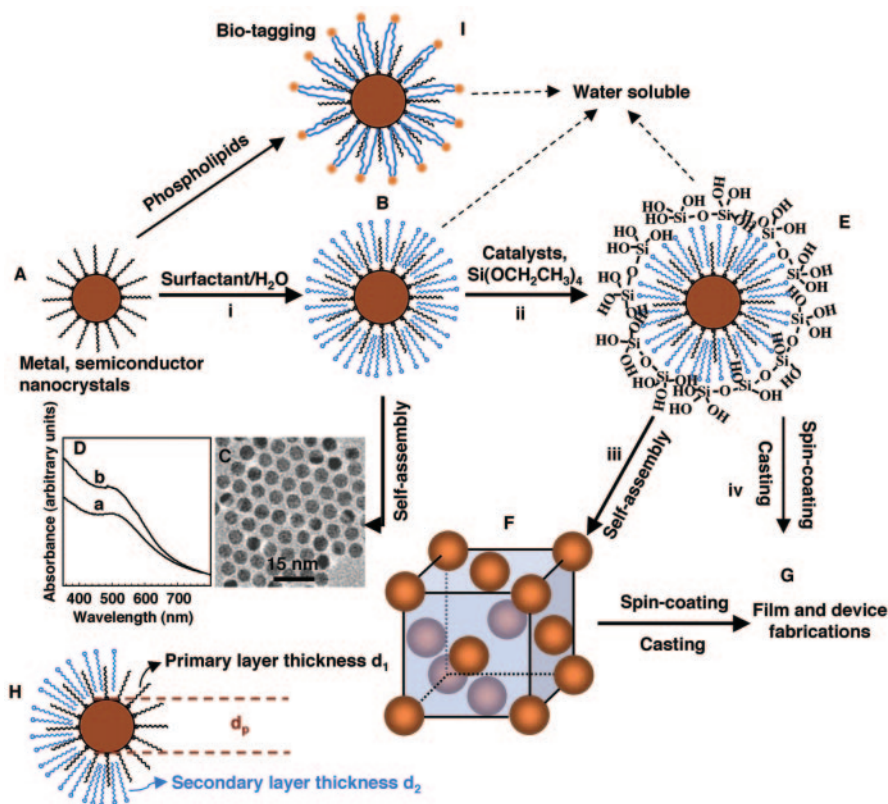


**Fig. 1.** Processing diagram for the synthesis of water-soluble gold nanocrystal micelles and periodically ordered gold NC/silica mesophases. (A) Gold nanocrystals were prepared according to the method of Brust *et al.* (15), with 1-DT as a stabilizing agent. Heat treatments were employed to further narrow the particle size distributions. (B) Thiol-stabilized nanocrystals are encapsulated in surfactants (using an oil-in-water microemulsion technique) (fig. S1) to form water-soluble NC micelles that, upon evaporation, self-assemble to form hexagonally ordered NC arrays as shown in the TEM image (C). (D) UV-visible spectra of (a) gold nanocrystals in chloroform and (b) gold NC micelles in water; both exhibit plasmon resonance bands at  $510\text{ nm}^{-1}$ . (E) Silicic acid moieties formed by hydrolysis of TEOS are organized at the hydrophilic surfactant-water interface of NC micelles, leading, under basic conditions, to a gold NC/silica mesophase (F) composed of NCs organized in a periodic FCC lattice within a dense silica matrix. (G) Under acidic conditions that suppress siloxane condensation, spin coating or casting results in ordered thin-film NC/silica mesophases that are readily integrated into devices. (H) The lattice constant of the NC/silica mesophase is controlled by the nanocrystal size,  $d_p$ , the primary layer thickness of the alkanethiol,  $d_1$ , and/or the secondary layer thickness of the surfactant,  $d_2$  (Fig. 2). (I) Polyethylene glycol surfactants or lipids can be used to prepare biocompatible water-soluble NC micelles for biolabeling (27).

forms within a limited NC/surfactant/silica compositional range as expected for a thermodynamically defined mesophase. In this case surfactant and gold are all incorporated into NC micelles, allowing the host framework to be essentially pure, dense silica (polysilicic acid). Highly ordered NC mesophases also require monosized NCs. A broad, poorly defined XRD pattern (Fig. 2A, curve e) was obtained for a gold NC/silica powder sample prepared as in Fig. 2A, curve b, but using gold NCs synthesized according to Brust *et al.* (15) and known to have a rather broad size distribution (~50% compared with ~5% in the present study).

As suggested by Fig. 1H, changing the primary NC particle size  $d_p$ , the primary layer thickness  $d_1$ , or the secondary layer thickness  $d_2$  allows adjustment of the NC mesophase lattice constant. For example, Fig. 2B shows the (111)  $d$ -spacing to change linearly from ~5.0 to 7.2 nm through variation of  $d_p$  from 1.0 to 3.3 nm. Figure 2C shows that changing the secondary layer thickness  $d_2$  by 4 carbon units [ $\text{CH}_3(\text{CH}_2)_n(\text{NCH}_3)_3^+\text{Br}^-$ ,  $n_l = 11$  to  $n_m = 15$ ] results in a 1.11-nm change in (111)  $d$ -spacing (1.38 Å/C-C bond), consistent with model predictions and structural studies.

In acidic conditions designed to minimize the siloxane condensation rate (pH ~2), pathway i-ii-iv (Fig. 1) leads to the formation of thin films using standard techniques like spin coating, micromolding, or ink-jet printing. By suppressing siloxane condensation and, thereby, gel formation, solvent evaporation accompanying coating induces self-assembly of NC micelles into NC thin-film mesophases (Fig. 3C) in a manner similar to the evaporation-induced self-assembly of cubic or hexagonal silica/surfactant thin-film mesophases (16). The thin-film XRD pattern (Fig. 2A, curve a) is consistent with a slightly distorted mesophase (face-centered tetragonal) due to constrained 1D shrinkage normal to the substrate surface, observed consistently for thin-film mesophases as a result of siloxane condensation (17). TEM images of films (e.g., Fig. 3C) are qualitatively similar to those of powders, although both XRD and TEM indicate a slightly reduced unit cell dimension ( $a \sim 9.6$  nm).

The metallic NC mesophases are highly ordered, fully 3D NC arrays. While several experimental investigations of transport in 1D and 2D ordered arrays have been reported (5, 7, 18), there are no comparable studies performed on high-quality 3D arrays.

As an initial investigation of charge transport, we fabricated planar metal-insulator-metal (MIM) devices, incorporating a Au NC/silica array as the insulator layer (see schematic in Fig. 4), and measured their temperature-dependent current-voltage ( $I$ - $V$ ) characteristics. Control samples were fabricated by spin coating gold-free silica

sols designed to form silica layers comparable to those of the silica matrices of the NC/silica films.

Samples were mounted on a cold finger, and direct current  $I$ - $V$  measurements were performed over the temperature range 300 K to 78 K. The  $I$ - $V$  curves for the gold NC/silica capacitors are plotted in Fig. 4A. At room temperature, the  $I$ - $V$  curve is linear with a zero-biased resistance of 14 M ohm, corresponding to a film resistivity of about  $3 \times 10^6$  ohm-cm. Nonlinearity in the  $I$ - $V$  behavior near zero bias is evident at 200 K and increases with decreasing temperature. At 100 K and below, conduction occurs through the gold NC/silica insulator only above a minimum threshold voltage,  $V_T$ , indicative of a collective Coulomb blockade (19) resulting from electrical isolation of the NCs. Comparison measurements on gold-free control samples showed no noticeable change in the  $I$ - $V$  characteristics over this temperature range.

Models of the (low voltage) electron transport in an array of identical Coulomb islands predict a thermally activated behavior of the zero-bias conductance,  $G_0 \propto \exp[-E_a/k_B T]$  (20), where  $E_a$  is the energy required to charge an electrically neutral nanocrystal and  $k_B$  is Boltzmann's constant. The Coulomb charging energy can be expressed as  $e^2/2C_0$ , where, for a completely isolated NC, the capacitance  $C_0$  depends on the product of the dielectric constant of the surrounding medium  $\epsilon$  and the nanocrystal radius  $r$ ,  $C_0 = 4\pi\epsilon_0\epsilon r$ . Using  $r \sim 1.5$  nm for the NC radius (determined by TEM) (Fig. 3A, inset a1) and  $\epsilon = 3.9$  for the surrounding silica matrix,  $C_0$  is calculated to be 0.7 aF, corresponding to a Coulomb charging energy of 123 meV.

The temperature-dependent conductance of the Au/silica NC array is presented in Fig. 4A (inset). We observe a strict Arrhenius behavior ( $G_0 \propto \exp[-E_a/k_B T]$ ) over the complete temperature range 78 K to 300 K, attesting to the particle/array uniformity. Two-dimensional NC arrays and granular films in general often show a  $G_0 \propto \exp[-(E_a/k_B T)^{1/2}]$  dependence caused by particle-size polydispersity (5, 20, 21). The experimental value of the charging energy,  $E_a = 90$  meV, determined from the slope in Fig. 4A (inset), is less than the prediction for an isolated NC.

The temperature-dependent conductance of the Au/silica NC array is presented in Fig. 4A (inset). We observe a strict Arrhenius behavior ( $G_0 \propto \exp[-E_a/k_B T]$ ) over the complete temperature range 78 K to 300 K, attesting to the particle/array uniformity. Two-dimensional NC arrays and granular films in general often show a  $G_0 \propto \exp[-(E_a/k_B T)^{1/2}]$  dependence caused by particle-size polydispersity (5, 20, 21). The experimental value of the charging energy,  $E_a = 90$  meV, determined from the slope in Fig. 4A (inset), is less than the prediction for an isolated NC.

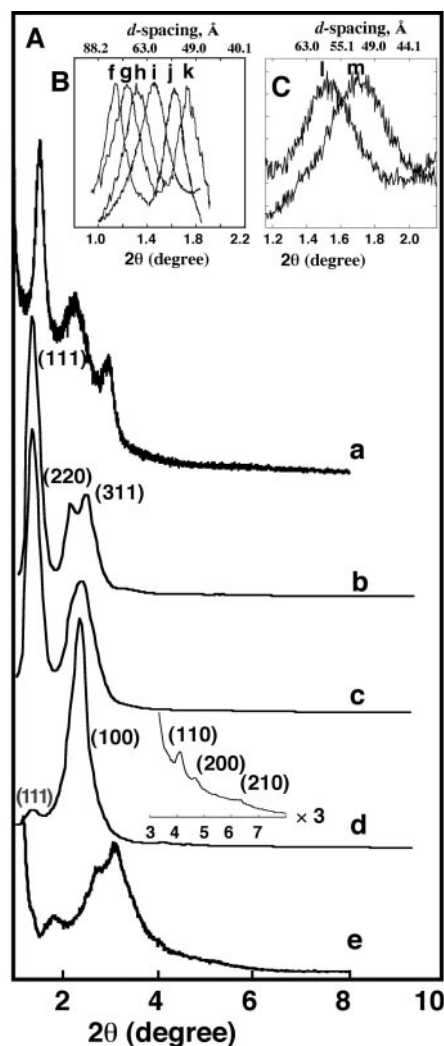


**Fig. 2.** (A) Representative XRD patterns of gold NC/silica mesophases. (a) Gold NC/silica thin-film mesophase formed by spin coating (Fig. 1, pathway i-ii-iv). The pattern can be indexed as an FCC mesostructure with lattice constant  $a = 95.5$  Å. The b, c, and d XRD patterns of bulk gold NC/silica samples were prepared according to pathway i-ii-iii (Fig. 1) by addition of NaOH to an aqueous solution containing TEOS and gold NC micelles. The weight percent of gold NC micelles was progressively reduced from b to d, while the TEOS/surfactant molar ratios were kept constant. (b) Sample was prepared by using 0.36 g 1-DT derivatized gold NCs. The pattern is consistent with an FCC mesostructure with lattice constant  $a = 102$  Å. (c) Sample was prepared by using 0.23 g 1-DT derivatized gold NCs. The pattern is similar to that of sample (b). However, the (220) and (311) reflections are not resolved. (d) Sample was prepared by using 0.12 g 1-DT derivatized gold NCs. The XRD pattern (inset magnified  $\times 3$ ) is indexed as a hexagonal silica mesophase with lattice constant  $a = 43.4$  Å. A small (111) peak attributable to the NC/silica mesophase is still observed. (e) Sample was prepared by using 0.36 g 1-DT derivatized gold NCs. These NCs were synthesized directly by the method of Brust *et al.* (15) without narrowing the particle size distribution. The amounts of TEOS and surfactant were the same as in b to d. The broader NC size distribution reduces considerably the extent of order. (B) Magnifications of the (111) reflections plotted linearly for samples prepared as in (A)(a), using gold NCs with successively smaller diameters (~33 Å, ~27 Å, ~23 Å, ~17 Å, ~12 Å, ~11 Å). (C) Magnifications of the (111) reflections plotted linearly for samples prepared as in (A)(b), with two different secondary alkane chain lengths of the surfactant [ $\text{CH}_3(\text{CH}_2)_n(\text{N}(\text{CH}_3)_3^+\text{Br}^-$ ,  $n_l = 15$ ,  $n_m = 11$ ].

## REPORTS

Presumably, this discrepancy reflects the reduction of the charging energy arising from the influence of the surrounding nanocrystals. For 2D NC arrays with sufficiently small NC spacings, both modeling and experiment show the charging energy to vary reciprocally with the number of nearest neighbors (5, 7).

Although 3D models of the NC charging energy have not been formulated, it is anticipated that interparticle capacitance could easily account for the 33-meV reduction in  $E_a$  observed here.

At low temperatures ( $T < 100$  K) where we observe Coulomb blockade behavior, the-

ory predicts that, for  $V > V_T$ , current scales as a power law,  $I = I_0(V/V_T - 1)^\zeta$ . The scaling exponent  $\zeta$  reflects the dimensionality of the accessible current-conducting pathways, and, for 1D and 2D, both modeling (5, 7) and experiment (22) show  $\zeta$  to equal approximately the array dimensionality. Figure 4B plots representative current-voltage scaling data for our 3D gold/silica NC arrays at 77 K. The results show power-law scaling with  $\zeta = 2.7$  (negative bias) and  $\zeta = 3.0$  (positive bias). Currently, there are no theoretical predictions or simulations of the 3D scaling exponent; however, the greater value of  $\zeta$  observed here, compared with previous studies of 2D (22) and quasi-3D arrays (5), is consistent with the greater number of conductive pathways expected for a fully 3D array.

The formation of water-soluble NC micelles and their self-assembly into ordered 3D mesophases provides a new means to integrate model 3D NC arrays into robust devices. The silica host matrix provides compatibility with standard microelectronics processing/patterning and helps eliminate parasitic conductive pathways, enabling higher temperature operation. We expect that by using more surfactant we could provide a mesoporous low  $k$  silica host (23), reducing the capacitance and allowing yet higher (i.e., room temperature) operation. The arrays we describe could be the ideal media for the study of the Hubbard Hamiltonian and the variety of transport and collective phenomena predicted to occur for such systems (24, 25). Beyond transport, these robust, highly ordered NC arrays could be useful for catalysts and photonic devices such as lasers (4, 26), and the water-soluble NC micelle intermediates have shown promise for biological labeling or sensors.

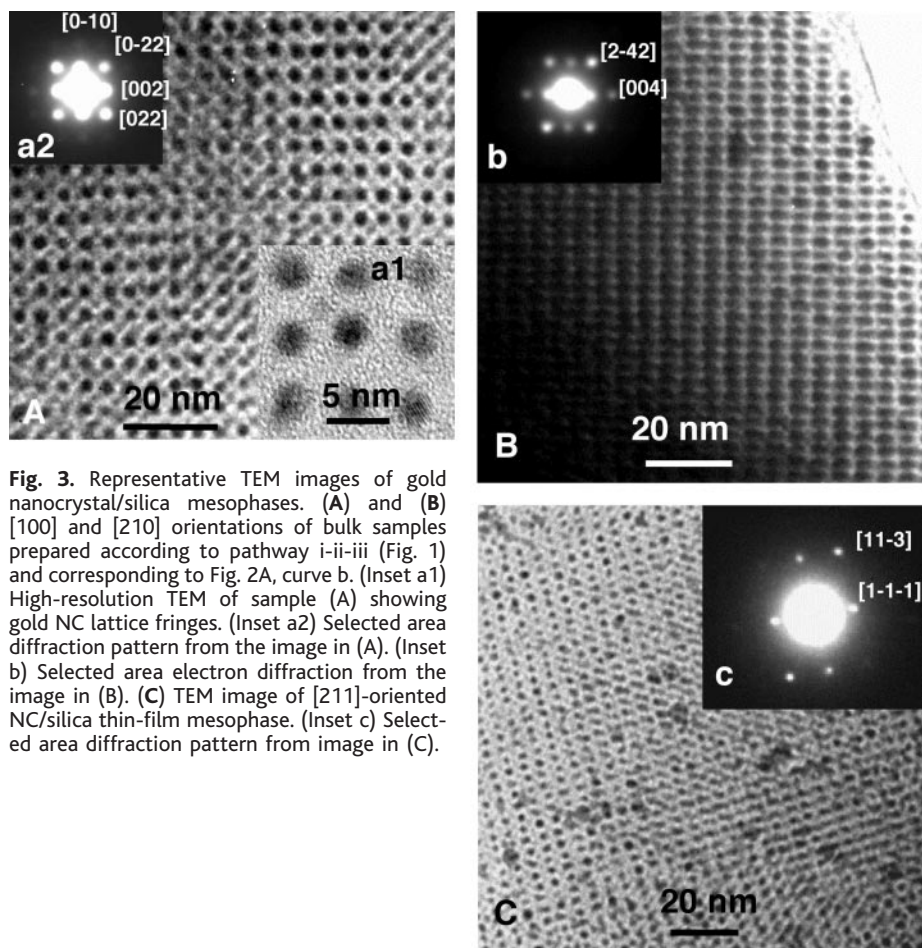


**Fig. 3.** Representative TEM images of gold nanocrystal/silica mesophases. (A) and (B) [100] and [210] orientations of bulk samples prepared according to pathway i-ii-iii (Fig. 1) and corresponding to Fig. 2A, curve b. (Inset a1) High-resolution TEM of sample (A) showing gold NC lattice fringes. (Inset a2) Selected area diffraction pattern from the image in (A). (Inset b) Selected area electron diffraction from the image in (B). (C) TEM image of [211]-oriented NC/silica thin-film mesophase. (Inset c) Selected area diffraction pattern from image in (C).

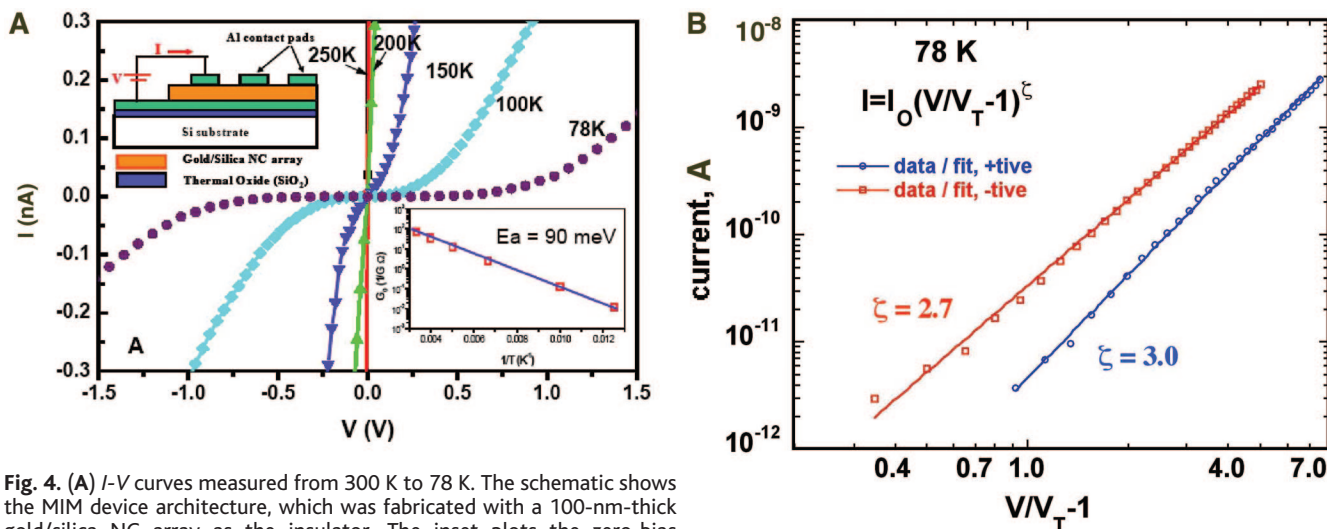


**Fig. 4.** (A)  $I$ - $V$  curves measured from 300 K to 78 K. The schematic shows the MIM device architecture, which was fabricated with a 100-nm-thick gold/silica NC array as the insulator. The inset plots the zero-bias conductance ( $G_0$ ) versus  $1/T$ . Data exhibit Arrhenius behavior with activation energy ( $E_a$ ) of  $\sim 90$  meV. (B) At  $T = 78$  K, current displays a power-law dependence for  $V > V_T$  with scaling exponent  $\zeta = 2.7$  (negative bias) and  $\zeta = 3.0$  (positive bias).  $V_T$  and  $\zeta$  were determined by the Levenberg-Marquardt nonlinear least squares method (28) (fig. S3).

## References and Notes

- M. A. El-Sayed, *Acc. Chem. Res.* **34**, 257 (2001).
- C. B. Murray, C. R. Kagan, M. G. Bawendi, *Annu. Rev. Mater. Sci.* **30**, 545 (2000).
- V. C. Sundar, H. J. Eisler, M. G. Bawendi, *Adv. Mater.* **14**, 739 (2002).
- M. A. Petruska, A. V. Malko, P. M. Voyles, V. I. Klimov, *Adv. Mater.* **15**, 610 (2003).
- C. T. Black, C. B. Murray, R. L. Sandstrom, S. H. Sun, *Science* **290**, 1131 (2000).
- M. Pileni, *J. Phys. Chem. B* **105**, 3358 (2001).
- A. A. Middleton, N. S. Wingreen, *Phys. Rev. Lett.* **71**, 3198 (1993).
- R. Parthasarathy, C. M. Lin, K. Elteto, T. F. Rosenbaum, H. M. Jaeger, *Phys. Rev. Lett.* **92**, 076801 (2004).
- M. Bruchez, M. Moronne, P. Gin, S. Weiss, A. P. Alivisatos, *Science* **281**, 2013 (1998).
- Details of the synthesis and characterizations are available on Science Online.
- J. Beck *et al.*, *J. Am. Chem. Soc.* **114**, 10834 (1992).
- C. B. Murray, C. R. Kagan, M. G. Bawendi, *Science* **270**, 1335 (1995).
- A. P. Alivisatos *et al.*, *Nature* **382**, 609 (1996).
- C. A. Mirkin, R. L. Letsinger, R. C. Mucic, J. J. Storhoff, *Nature* **382**, 607 (1996).
- M. Brust, M. Walker, D. Bethell, D. J. Schiffrin, R. Whyman, *J. Chem. Soc. Chem. Commun.* **1994**, 801 (1994).
- Y. Lu *et al.*, *Nature* **389**, 364 (1997).
- D. A. Doshi *et al.*, *Science* **290**, 107 (2000).
- C. P. Collier, R. J. Saykally, J. J. Shiang, S. E. Henrichs, J. R. Heath, *Science* **277**, 1978 (1997).
- H. Grabert, M. H. Devoret, *Single Charge Tunneling* (Plenum, New York, 1992).
- C. A. Neugebauer, M. B. Webb, *J. Appl. Phys.* **33**, 74 (1961).
- D. L. Peng, K. Sumiyama, S. Yamamuro, T. Hihara, T. J. Konno, *Appl. Phys. Lett.* **74**, 76 (1999).
- A. J. Rumberg, T. R. Ho, J. Clarke, *Phys. Rev. Lett.* **74**, 4714 (1995).
- Y. F. Lu *et al.*, *J. Am. Chem. Soc.* **122**, 5258 (2000).
- C. A. Stafford, S. Das Sarma, *Phys. Rev. Lett.* **72**, 3590 (1994).
- G. Kirczenow, *Phys. Rev. B Condens. Matter* **46**, 1439 (1992).
- V. I. Klimov *et al.*, *Science* **290**, 314 (2000).
- B. Dubertret *et al.*, *Science* **298**, 1759 (2002).
- W. H. Press, B. P. Flannery, S. A. Teukolsky, W. T. Vetterling, *Numerical Recipes* (Cambridge Univ. Press, Cambridge, UK, 1986), chap. 14.
- We thank V. Klimov and M. Petruska at Los Alamos National Laboratory for providing CdSe nanocrystals and useful discussions. T. Rieker, NSF (formerly University of New Mexico), performed early XRD experiments. This work was partially supported by the U.S. Department of Energy (DOE) Basic Energy Sciences Program, the Army Research Office, Sandia National Laboratory's Laboratory Directed R&D program and Center for Integrated Nanotechnologies, and the Air Force Office of Scientific Research. TEM investigations were performed in the Department of Earth and Planetary Sciences at the University of New Mexico. Sandia is a multiprogram laboratory operated by Sandia Corporation, a Lockheed Martin Company, for DOE under contract DE-AC04-94ALB5000.

## Supporting Online Material

www.sciencemag.org/cgi/content/full/304/5670/567/DC1

Materials and Methods

Figs. S1 to S3

29 December 2003; accepted 17 March 2004

# Probabilistic Integrated Assessment of "Dangerous" Climate Change

Michael D. Mastrandrea<sup>1\*</sup> and Stephen H. Schneider<sup>2</sup>

Climate policy decisions are being made despite layers of uncertainty. Such decisions directly influence the potential for "dangerous anthropogenic interference with the climate system." We mapped a metric for this concept, based on Intergovernmental Panel on Climate Change assessment of climate impacts, onto probability distributions of future climate change produced from uncertainty in key parameters of the coupled social-natural system—climate sensitivity, climate damages, and discount rate. Analyses with a simple integrated assessment model found that, under midrange assumptions, endogenously calculated, optimal climate policy controls can reduce the probability of dangerous anthropogenic interference from ~45% under minimal controls to near zero.

Article 2 of the United Nations Framework Convention on Climate Change (UNFCCC) states its ultimate objective as "Stabilization of greenhouse gas concentrations in the atmosphere at a level that would prevent dangerous anthropogenic interference with the climate system" (1). This level should be achieved within a time frame sufficient to allow ecosystems to adapt naturally to climate change, to ensure that food production is not threatened, and to enable economic development to proceed in a sustainable manner. Thus, the criteria for identifying "dangerous anthropogenic interference" (DAI) may be characterized in terms of the consequences (or impacts) of climate change (2). Although these impacts, and a precise definition of DAI, are subject to considerable uncertainty, a plausible

uncertainty range can be quantified from current scientific knowledge (3). We argue that climate change policy decisions should be conceptualized in terms of preventing or reducing the probability of DAI, a risk-management framework familiar to policymakers and an outcome to which more than 190 signatories to the UNFCCC have committed.

Research related to global climate change must deal explicitly with uncertainty about future climate impacts. Due to the complexity of the climate change issue and its relevance to international policymaking, careful consideration and presentation of uncertainty is important when communicating scientific results (2, 4–7). Policy analysis regarding climate change necessarily requires decision-making under uncertainty (8–10). Without explicit efforts to quantify the likelihood of future events, users of scientific results (including policy-makers) will undoubtedly make their own assumptions about the probability of different outcomes, possibly in ways that the original authors did not intend (11, 12).

Assigning likelihoods to potential future worlds is difficult, as noted by Gröbler and Nakicenovic (13), because any such estimates will be highly subjective and based on assessments of future societal behavior and values. Uncertainty, they warn, may alternatively be dismissed or replaced by spurious expert opinion. Although the suitability and effectiveness of techniques for presenting uncertain results is context-dependent, we believe that such probabilistic methods are more valuable for communicating an accurate view of current scientific knowledge to those seeking information for decision-making than assessments that do not attempt to present results in probabilistic frameworks (14).

We present a metric for assessing DAI: a cumulative density function (CDF) of the threshold for dangerous climate change. We demonstrate its utility by applying it to modeled uncertainty in future climate change using an optimizing integrated assessment model (IAM). IAMs are common policy analysis tools that couple submodels of the climate and economic systems, balance costs and benefits of climate change mitigation to determine an "optimal" policy (15), and often exhibit properties not apparent in either submodel alone (16).

We chose Nordhaus' Dynamic Integrated Climate and Economy (DICE) model (17) for our analysis because of its relative simplicity and transparency, despite its limitations (16, 18). The IAM framework allows us to explore the effect of a wide range of mitigation levels on the potential for exceeding a policy-important threshold such as DAI. We do not recommend that our quantitative results be taken literally, but we suggest that our probabilistic framework and methods be taken seriously. They produce general conclusions that are more robust than estimates made with a limited set of scenarios or without probabilistic presentations of outcomes, and our threshold metric for DAI offers a risk-man-

<sup>1</sup>Interdisciplinary Graduate Program in Environment and Resources, <sup>2</sup>Department of Biological Sciences and Center for Environmental Science and Policy, Stanford University, Stanford, CA 94305, USA.

\*To whom correspondence should be addressed. E-mail: mikemas@stanford.edu